Competition between line tension and curvature stabilizes modulated phase patterns on the surface of giant unilamellar vesicles: A simulation study

Jonathan J. Amazon,[*] Shih Lin Goh,[†] and Gerald W. Feigenson[‡]
Department of Molecular Biology and Genetics, Cornell University, Ithaca, New York
(Received 30 September 2012; revised manuscript received 27 November 2012; published 13 February 2013)

When prepared in the liquid-liquid coexistence region, the four-component lipid system distearoyl-phosphatidylcholine–dioleoyl-phosphatidylcholine–palmitoyl,oleoyl-phosphatidylcholine–cholesterol (DSPC-DOPC-POPC-Cholesterol), with certain ratios of DOPC and POPC, shows striking modulated phase patterns on the surface of giant unilamellar vesicles (GUVs). In this simulation study, we show that the morphology of these patterns can be explained by the competition of line tension (which tends to favor large round domains) and curvature, as specified by the Helfrich energy functional. In this study we use a Monte-Carlo simulation on the surface of a GUV to determine the equilibrium shape and phase morphology. We find that the patterns arising from these competing interactions very closely approximate those observed, that the patterned morphologies represent thermodynamically stable configurations, and that the geometric nature of these patterns is closely tied to the relative and absolute values of the model parameters.

DOI: 10.1103/PhysRevE.87.022708 PACS number(s): 87.16.dt, 87.16.af, 87.16.aj

I. INTRODUCTION

Model systems provide an important way to study and understand the behavior of multicomponent lipid bilayer membranes. The three-component lipid system distearoyl-phosphatidylcholine–dioleoyl-phosphatidylcholine–cholesterol (DSPC-DOPC-Cholesterol) has a well-characterized phase diagram, with a region of liquid-liquid ($L_o + L_d$) coexistence that is readily observable in giant unilamellar vesicle (GUV) studies as large round domains [1,2]. This mixture is a useful model for understanding the general nature of bilayers containing a high melting lipid (DSPC), a low melting lipid (DOPC), and cholesterol.

If we replace the low melting lipid, DOPC, with POPC (palmitoyl, oleoyl-phosphatidylcholine), we find a stark difference in the phase morphology. Performing GUV imaging studies on the POPC-containing system reveals that the liquid-liquid coexistence region appears uniform, unlike the macroscopic phase domains seen with DOPC-containing mixtures. However, FRET, ESR [3], and neutron scattering studies [4] show that liquid-liquid coexistence is present with POPC. This observation implies that phase separation occurs in the POPC-containing system on the nanometer scale, thus not resolvable by ordinary light microscopy. Given the large body of data from studies of animal cell plasma membranes that supports the occurrence of $L_o + L_d$ phase domains [5–7], and given that the size scale, shapes, and connectivities of phase-separated domains might be involved in the fundamental behaviors of animal cells, understanding the membrane in terms of a nonrandom physical mixture might be important.

A four-component mixture containing DSPC, DOPC, POPC, and cholesterol enables study of the full range of phase morphologies, from domain size scale of nanometers to microns, that could occur in cell membranes. On the DOPC-heavy side of this phase diagram we expect large macroscopic domains, whereas on the POPC-heavy side we expect GUVs to appear uniform (nanodomains). The relative amounts of DOPC and POPC can be controlled precisely in order to study the macro-to-nano transition [8]. The relative amount of DOPC and POPC can be described by ρ, given as,

$$\rho \equiv \frac{\chi_{\mathrm{DOPC}}}{\chi_{\mathrm{DOPC}} + \chi_{\mathrm{POPC}}}, \tag{1}$$

where χ_{DOPC} and χ_{POPC} are the mole fractions of DOPC and POPC, respectively. In this way, $\rho = 1.00$ corresponds to a three-component mixture with DOPC as the only low-melting component and $\rho = 0.00$ corresponds to a three-component mixture with POPC as the only low-melting component. The trajectory defined by varying ρ from 0.00 to 1.00 pierces the tetrahedral composition space, with endpoints located on the POPC and DOPC faces. For both experimental and simulation studies, the mole fractions of DSPC and CHOL are held fixed unless otherwise stated.

When DSPC and CHOL are held at particular mole fractions within the liquid-liquid coexistence region, for example, $\chi_{\mathrm{DSPC}} = 0.45$ and $\chi_{\mathrm{CHOL}} = 0.25$, and the value of ρ is varied, a patterning of the phases is observed in the composition range, $0.15 < \rho < 0.25$ [8]. This range can be termed the "modulated phase window" and for these particular compositions is characterized by thin stripes of L_d phase within a more abundant L_o phase, as shown in Fig. 1. The overall pattern can resemble striped or honeycomb-like structures, each with a characteristic periodicity. For this particular composition ($\chi_{\mathrm{DSPC}} = 0.45, \chi_{\mathrm{CHOL}} = 0.25$), macroscopic domains are observed when $\rho > 0.25$ and uniform GUVs are observed when $\rho < 0.15$ [8].

The underlying mechanism of the formation of modulated phases in this system has not previously been understood. Our aim is to model and simulate the formation of these modulated phases to better understand the transition taking place as mixture composition moves through this ρ window. We can then use this model to make predictions about the nature of nanodomains present in the pure POPC system and eventually the nature of phase separation on the plasma membrane.

[*]jja54@cornell.edu
[†]sg367@cornell.edu
[‡]gwf3@cornell.edu

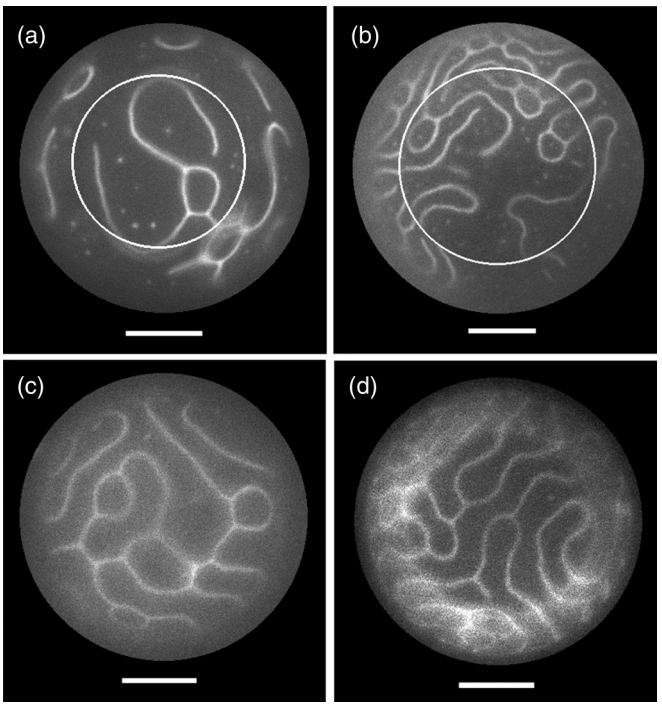

FIG. 1. Four examples of modulated phase patterns observed using wide-field fluorescence microscopy. Images are cropped and contrast adjusted. (a) and (b), composite images of focused slices of the GUV, the white ring marking the boundary of the composite image. GUV compositions DSPC-DOPC-POPC-Chol: (a) 0.487/0.0625/0.188/0.263, (b) 0.45/0.075/0.225/0.25, (c) and (d) 0.395/0.12/0.18/0.305. Dye C12:0 DiI (0.02 mol%) partitions into L_d. Scale bars, 10 μm, temperature 23°C.

II. MATERIALS AND METHODS

A. GUV preparation and microscopy

GUV samples were prepared as described in Ref. [8] with the following modifications: GUVs were swelled at 55°C in either 100 mM sucrose or 100 mM glucose and then cooled to room temperature (23°C) over 12 h. Samples were harvested into microcentrifuge tubes (Fisher Scientific) using large orifice pipet tips (Fisher Scientific) and then let settle for about 2 h before observation.

Widefield microscopy was performed on a Nikon Diaphot-TMD inverted microscope at 23°C using a 60× 1.4NA oil immersion objective. To minimize light-induced artifacts, GUVs were first located in bright field mode before illumination for fluorescence. Samples contained 0.02 mol% C12:0 DiI, imaged with 535- to 550-nm excitation and 565- to 610-nm emission. Images were collected with a Photometrics charge-coupled device camera CoolSNAPHQ2 (Tucson, Arizona).

Phospholipids were purchased from Avanti Polar Lipids (Alabaster, AL), cholesterol from Nu Chek Prep (Elysian, MN), and the fluorescent dye C12:0-DiI (1,1′-didodecyl-3,3,3′,3′-tetramethylindocarbocyanine perchlorate) from Invitrogen (Carlsbad, CA). Concentrations of phospholipid stocks were determined to <1% error with inorganic phosphate assay [9], and purity checked with thin layer chromatography in chloroform-methanol-water solvent. Cholesterol at defined concentration was prepared by standard gravimetric procedures. Fluorescent dye concentrations were determined using absorption spectroscopy on an HP 8452A spectrophotometer (Hewlett-Packard, Palo Alto, CA).

B. Simulation model

To approach the problem of explaining the appearance of modulated phases, we constrain our model of the observed patterns in two ways:

(1) Modulated phases are at a state of thermodynamic equilibrium. This is supported by the observation that the patterns do not change over the observation times, persisting for hours and even days.

(2) Bilayers are phase-separated, the two coexisting phases are fluid, and the value of ρ changes only the material parameters describing the energetics of that phase. These assumptions are reasonable because the compositions under consideration are squarely within the liquid-liquid coexistence region of both of the $\rho = 0.00$ and $\rho = 1.00$ faces of the phase diagram tetrahedron [3]. This simplifies the mathematical model, as we can drop terms in the energy functional that are not related to morphology (such as any term that depends only on the local composition).

Our approach uses a competing interactions model [10], which has been shown to produce modulated phases in many systems. The formalism states that multiple fields (order parameters) that couple in a way that opposes the formation of a single domain with minimal boundary can form equilibrium honeycomb and striped patterns.

The fields we consider are the local composition and the local curvature of the membrane [11–13]. These couple through the composition-dependent material properties [14–18], which dictate the energetics of bending and stretching the membrane. We implement this model in simulation to find the thermodynamic equilibrium state. To do so we use a Monte-Carlo simulation to sample the configuration space of fields, then we use the Metropolis Algorithm [12] to ensure that energy is minimized to within thermal noise.

Similar simulations have been performed, including the work of Lipowsky *et al.*, which showed how curvature and line tension were able to stabilize as many as seven domains and give rise to a variety of GUV shapes [12]. Simulation studies of Fan *et al.* showed that more complicated models, such as lipid recycling, can stabilize nonequilibrium patterns on a flat membrane [19]. Other models for the stabilization of multiple and patterned domains have also been studied, including a general competing interaction model [20] and the effects of dipolar repulsion between lipids [21–23]. It has been shown that electrostatics are too short-range to account for the many micron length scale we observe in modulated phases [8].

To begin modeling the modulated phases, we first formulate an energy functional. The three fields that our energy functional depends on are the local phase, ϕ, the mean curvature, H, and the Gaussian curvature G.

C. Local phase field

The local phase at a point, r, on the membrane surface is given by the $\phi(r)$ field,

$$\phi(r) = \begin{cases} 0 & r \in L_d \\ 1 & r \in L_o. \end{cases} \tag{2}$$

This binary field allows us to define the phase morphology on the surface. We also assume that the total amount of each phase is fixed (that is, we choose where we are along a given thermodynamic tie line). If we specify the fraction of surface in the L_o phase by P, then this constraint can be written

$$\frac{1}{A_{\text{tot}}} \iint \phi(r) dA = P, \tag{3}$$

where A_{tot} is the total area of the membrane surface. The value of A_{tot} is also considered fixed because of the large elastic modulus of lipid bilayers [12,17,24].

D. Mean curvature field

The mean curvature can be defined as the divergence of the surface normals,

$$H(r) = \nabla \cdot \vec{n}(r), \tag{4}$$

which means that mean curvature can roughly be interpreted as the degree to which the normal vectors point toward ($H < 0$) or away from ($H > 0$) each other. For computational purposes, we use an alternative definition of the mean curvature relating to the change in area under normal projection:

If each point in a small patch of area A is projected outwards a distance ΔR along the surface normals, then the change in area ΔA is related to the mean curvature by

$$\Delta A = A H(r) \Delta R, \tag{5}$$

which can be rearranged to give an explicit expression for $H(r)$,

$$H(r) = \frac{\Delta A}{A \Delta R}. \tag{6}$$

This is known as the first variation of area formula, which lends itself easily to a general method for calculating curvature fields on a discrete surface. A diagram of this process is shown in Fig. 4.

E. Gaussian curvature field

The Gaussian curvature can be locally defined by the Gauss-Bonnet theorem. Consider a small N-sided polygon with area A, centered on a point r, that is delimited by surface geodesics that meet at exterior angles θ_1, θ_2,...,θ_N. The Gaussian curvature at r is

$$G(r) = \frac{1}{A}\left[2\pi - \sum_{i=1}^{N} \theta_i\right]. \tag{7}$$

Gaussian curvature is roughly a measure of the extent to which parallel lines drawn on the surface are bent toward each other ($G > 0$) or away from each other ($G < 0$).

F. Energy functional

Since we assume that the membrane is already phase separated, our Hamiltonian has three major contributions [12,24]: the line tension term, $\mathcal{H}_P$, the mean curvature term, $\mathcal{H}_H$, and the Gaussian curvature term, $\mathcal{H}_G$. Thus, the Hamiltonian is expressed as

$$\mathcal{H}[\phi, H, G] = \mathcal{H}_P + \mathcal{H}_H + \mathcal{H}_G. \tag{8}$$

1. Line tension term ($\mathcal{H}_P$)

The line tension is an expression of the unfavorable energy required to make an interface between the two membrane phases [8,16,25]. It is defined by multiplying the total perimeter of the phase boundary, L, by a constant energy per unit length, γ,

$$\mathcal{H}_P = \gamma L. \tag{9}$$

It can be shown that for a fixed amount of L_d and L_o phases, the minimal boundary is achieved when one large round domain is formed, maximizing the area-to-perimeter ratio. This drives the system toward macroscopic phase separation.

To determine the value of L strictly from the function $\phi(r)$ is the product of a complicated limiting process. In practice, L is computed discretely and takes on the form of a simple sum.

2. Mean curvature term ($\mathcal{H}_H$)

The mean curvature and Gaussian curvature terms are both from the Helfrich formulation [12,24]. This defines the energy of bending the membrane up to quadratic order in the mean and Gaussian curvatures. The mean curvature expression is given by

$$\mathcal{H}_H = \iint \kappa[\phi(r)][H(r)]^2 dA, \tag{10}$$

where $\kappa(\phi)$ is the local bending modulus. This is defined as

$$\kappa(\phi) = \begin{cases} \kappa_d & \phi = 0 \\ \kappa_o & \phi = 1, \end{cases} \tag{11}$$

where κ_d and κ_o are the bending modulus in the L_d and L_o phases, respectively.

3. Gaussian curvature term ($\mathcal{H}_G$)

The Gaussian curvature term is also from the Helfrich functional and is defined as

$$\mathcal{H}_G = \iint \bar{\kappa}[\phi(r)] G(r) dA, \tag{12}$$

where $\bar{\kappa}(\phi)$ is defined similarly as

$$\bar{\kappa}(\phi) = \begin{cases} \bar{\kappa}_d & \phi = 0 \\ \bar{\kappa}_o & \phi = 1, \end{cases} \tag{13}$$

where $\bar{\kappa}_d$ and $\bar{\kappa}_o$ are the Gaussian bending modulus in the L_d and L_o phases, respectively.

4. Constraints

In addition to the three terms outlined above, we also include two harmonic constraint terms to keep the area and volume of the GUV close to a fixed value (defined at the outset of the simulation):

$$\mathcal{H}_A = A_l(A_{\text{tot}} - A)^2, \tag{14}$$

$$\mathcal{H}_V = V_l(V_{\text{tot}} - V)^2, \tag{15}$$

where A_{tot} and V_{tot} are the fixed values of the area and volume, respectively. The harmonic strengths A_l and V_l are in practice kept very large to allow very little fluctuation [12].

III. DISCRETE MODEL

The formalism outlined above is the continuum description of a phase-separated membrane's energetics. In order to simulate this system it is necessary to find a suitable discretization scheme that will allow us to faithfully mimic the conformations of a continuum membrane. To do this we use a triangulated lattice with an overall spherical topology [12].

This lattice can be described by a set of vertices, edges, and faces ($\{v_i\}$,$\{e_i\}$, and $\{f_i\}$) with N_v,N_e, and N_f elements, respectively. The number of vertices, edges, and faces also must satisfy the Euler characteristic of a sphere, $N_v - N_e + N_f = 2$. To define the topology, we must define the connectivity of the lattice. With n_i the number of neighbors that v_i[1] has (between 3 and 10), we define the three sets

$$\{v_{ij}\} \quad \{e_{ij}\} \quad \{f_{ij}\},$$

where v_{ij} is the jth neighbor of vertex i. It is important to note that the sequence of vertices defined by

$$v_{i0} \to v_{i1} \to \cdots \to v_{i(n_i-1)} \to v_{i0}$$

forms a counter clockwise loop around the parent vertex, v_i. The elements of $\{e_{ij}\}$ define the edges connecting the vertices v_i and v_{ij}. The elements of $\{f_{ij}\}$ define the faces containing the vertices v_i, v_{ij}, and $v_{i(j+1)}$. These elements are only defined for $0 \leqslant i < N_v$ and $0 \leqslant j < n_i$. The second index, j, is assumed to be modulo n_i unless stated otherwise. This geometric construction is shown in Fig. 2.

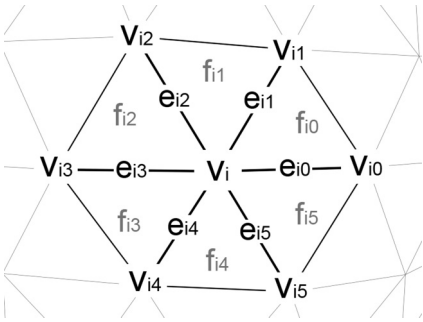

FIG. 2. Geometric layout of a vertex and its neighboring vertices, edges, and faces. The sequence of neighbors form a counter-clockwise loop allowing us to orient the surface normals outward.

A. Geometric properties

It is also useful to have the geometric parameters of the lattice at our disposal. Let f_i be a face delimited by the three vertices $\{\vec{w}_1,\vec{w}_2,\vec{w}_3\}$. The midpoint, normal, area, and volume associated with this face can all be defined from the geometry as

$$\vec{m}(f_i) = \tfrac{1}{3}(\vec{w}_1 + \vec{w}_2 + \vec{w}_3) \tag{16}$$

$$\vec{n}(f_i) = \frac{(\vec{w}_2 - \vec{w}_1) \times (\vec{w}_3 - \vec{w}_1)}{\|(\vec{w}_2 - \vec{w}_1) \times (\vec{w}_3 - \vec{w}_1)\|} \tag{17}$$

$$A(f_i) = \frac{\|(\vec{w}_2 - \vec{w}_1) \times (\vec{w}_3 - \vec{w}_1)\|}{2} \tag{18}$$

$$V(f_i) = \frac{A(f_i)[\vec{w}_1 \cdot \vec{n}(f_i)]}{3}. \tag{19}$$

The volume, $V(f_i)$, is the volume of the pyramid formed by connecting its three vertices to the origin. Similarly, let e_i be an edge delimited by the vertices $\vec{w}_1,\vec{w}_2$ and shared between the two faces g_1,g_2. The midpoint, normal, and length associated with this edge are defined as

$$\vec{m}(e_i) = \frac{\vec{w}_1 + \vec{w}_2}{2} \tag{20}$$

$$\vec{n}(e_i) = \frac{A(g_1)\vec{n}(g_1) + A(g_2)\vec{n}(g_2)}{\|A(g_1)\vec{n}(g_1) + A(g_2)\vec{n}(g_2)\|}. \tag{21}$$

$$L(e_i) = \|\vec{w}_2 - \vec{w}_1\|. \tag{22}$$

The normal, $\vec{n}(e_i)$, is the area weighted sum of the normals of the two adjacent faces. We may then define the normal, area, and volume associated with the vertex v_i as weighted sums over the adjacent faces,

$$\vec{n}(v_i) = \frac{\sum_{j=0}^{n_i-1} A(f_{ij})\vec{n}(f_{ij})}{\left\| \sum_{j=0}^{n_i-1} A(f_{ij})\vec{n}(f_{ij}) \right\|}, \tag{23}$$

$$A(v_i) = \frac{1}{3}\sum_{j=0}^{n_i-1} A(f_{ij}), \tag{24}$$

$$V(v_i) = \frac{1}{3}\sum_{j=0}^{n_i-1} V(f_{ij}). \tag{25}$$

Last, we define the perimeter to be interpolated between two adjacent vertices, v_i and v_{ij},

$$P_{ij} = \|\vec{m}(e_{ij}) - \vec{m}(f_{i(j-1)})\| + \|\vec{m}(f_{ij}) - \vec{m}(e_{ij})\|. \tag{26}$$

The fields are defined only on the vertices of the lattice. For brevity we refer to the values of ϕ,H,G on the vertex v_i as ϕ_i,H_i,G_i. To implement the energy functional outlined in the previous section, we could compute the values of each term on a discrete lattice. For the simulation, it is more useful to compute the local contributions to the energy from each vertex. The global energy can then be computed as a sum over all vertices.

[1]The symbol v_i refers to the scalar index of the vertex, while the symbol $\vec{v}_i$ refers to the vector position of the vertex.

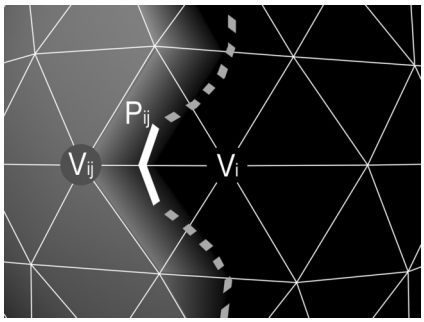

FIG. 3. Close-up of the boundary between the two phases: gray, L_d phase; black, L_o phase. The discrete interpolated boundary is shown dashed. The interpolated boundary between two adjacent vertices (v_i and v_{ij}) is shown in thick white, P_{ij}.

B. Discrete line tension

To compute the line tension contribution at the vertex v_i, we sum up the contributions to the boundary from each vertex and its neighbors,

$$L_i = \sum_{j=0}^{n_i-1} \left(1 - \delta_{\phi_i \phi_{ij}}\right) P_{ij}, \tag{27}$$

where the Kronecker δ ensures that only portions of boundary for which the adjacent vertices have opposite phase are counted. The contour used to interpolate the phase interface is shown in Fig. 3. The line tension contribution of vertex v_i is then

$$\mathcal{H}_P(v_i) = \gamma L_i. \tag{28}$$

C. Discrete mean curvature

The mean curvature, H_i, is calculated on each vertex using a discrete approximation to the first variation of area formula. The disk-shaped region around the vertex with initial area $A(v_i)$ is projected out a distance ΔR along the normals of the edges, as shown in Fig. 4. Let the two faces $g_{ij}^{(1)}$ and $g_{ij}^{(2)}$ be defined by the three points,

$$g_{ij}^{(1)} \equiv \{\vec{v}_i, \vec{m}(f_{i(j-1)}), \vec{m}(e_{ij})\}, \tag{29}$$

$$g_{ij}^{(2)} \equiv \{\vec{v}_i, \vec{m}(e_{ij}), \vec{m}(f_{ij})\}. \tag{30}$$

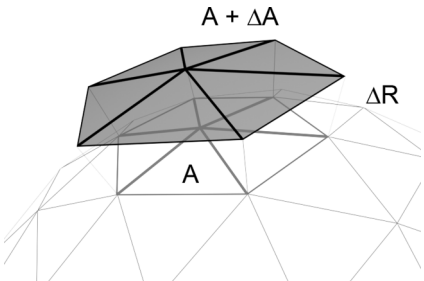

FIG. 4. The process of mean curvature computation. The initial star-shaped region around a vertex is projected along the surface normals a distance ΔR to produce the shaded gray umbrella region with a difference in area ΔA.

The projected faces $G_{ij}^{(1)}$ and $G_{ij}^{(2)}$ are given by

$$G_{ij}^{(1)} \equiv \{\vec{v}_i + \Delta R\vec{n}(v_i), \vec{m}(f_{i(j-1)}) + \Delta R\vec{n}(f_{i(j-1)}), \vec{m}(e_{ij}) + \Delta R\vec{n}(e_{ij})\}, \tag{31}$$

$$G_{ij}^{(2)} \equiv \{\vec{v}_i + \Delta R\vec{n}(v_i), \vec{m}(e_{ij}) + \Delta R\vec{n}(e_{ij}), \vec{m}(f_{ij}) + \Delta R\vec{n}(f_{ij})\}. \tag{32}$$

The change in area under projection can then be defined as a sum of the change in area of each face:

$$\Delta A = \sum_{j=0}^{n_i-1} \left[A\left(g_{ij}^{(1)}\right) - A\left(G_{ij}^{(1)}\right) + A\left(g_{ij}^{(2)}\right) - A\left(G_{ij}^{(2)}\right)\right]. \tag{33}$$

Now the mean curvature can be defined as

$$H_i = \frac{\Delta A}{A(v_i)\Delta R}. \tag{34}$$

The mean curvature term of the energy functional can now be defined on this vertex as

$$\mathcal{H}_H(v_i) = \kappa(\phi_i) H_i^2 A(v_i). \tag{35}$$

D. Discrete Gaussian curvature

The Gaussian curvature field is calculated by taking the angle deficit of the star-shaped region around a given vertex [12], v_i, as shown in Fig. 5. With the angle between two edges given by $e_i \angle e_j$, the angle deficit and Gaussian curvature can be written as

$$\theta_{ij} = [e_{ij} \angle e_{i(j+1)}], \tag{36}$$

$$G_i = \frac{2\pi - \sum_{j=0}^{n_i-1} \theta_{ij}}{A(v_i)}. \tag{37}$$

The Gaussian curvature term of the energy functional is now given by

$$\mathcal{H}_G(v_i) = \bar{\kappa}(\phi_i) G_i A(v_i). \tag{38}$$

E. Additional constraints

In addition to the three terms of our Hamiltonian, we must also include constraint terms that keep the discrete model from

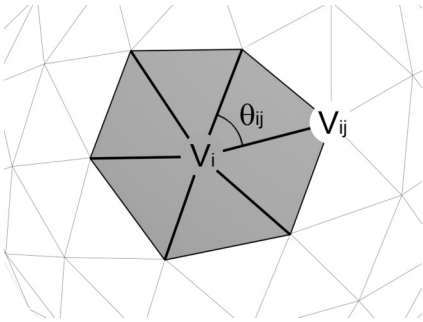

FIG. 5. Process of Gaussian curvature computation. The angle between adjacent edges is summed around a given vertex to compute the angle deficit.

taking on impossible configurations. There are five additional constraints we must impose on the lattice:

The areas of individual triangles on the surface are constrained to vary not too far from their initial value. Let $A_0(f_i)$ be the initial area of the face f_i. The local area constraint is

$$\mathcal{C}_A(f_i) = \begin{cases} 0 & |\Delta A(f_i)| \leqslant a_l A_0(f_i) \\ \infty & |\Delta A(f_i)| > a_l A_0(f_i) \end{cases}, \tag{39}$$

where $\Delta A(f_i) = A(f_i) - A_0(f_i)$. The parameter a_l gives the maximal wiggle room of the triangles as a fraction of its initial area; $a_l = 0$ implies a rigid lattice.

The length of the edges is also constrained in a similar manner [12]. Let $L_0(e_i)$ be the initial length of a given edge, e_i. The local edge length constraint is

$$\mathcal{C}_e(e_i) = \begin{cases} 0 & |\Delta L(e_i)| \leqslant e_l L_0(e_i) \\ \infty & |\Delta L(e_i)| > e_l L_0(e_i), \end{cases} \tag{40}$$

where $\Delta L(e_i) = L(e_i) - L_0(e_i)$. Again, the parameter e_l gives a wiggle room as a fraction of the initial length of that edge.

The next constraint is a convexity constraint on the shape of the closed surface. This constrains the normal vector of any face to lie within the 45° cone about the vector connecting the midpoint to the origin,

$$\mathcal{C}_n(f_i) = \begin{cases} 0 & [\vec{m}(f_i)\angle\vec{n}(f_i)] \leqslant \pi/4 \\ \infty & [\vec{m}(f_i)\angle\vec{n}(f_i)] > \pi/4. \end{cases} \tag{41}$$

This keeps the faces from flipping over and contributing negative volume to the calculations. Notice that each of these constraints are defined on the faces and edges. They can be redefined on the vertices of the lattice as sums over the neighboring faces and edges of that vertex,

$$\mathcal{C}_A(v_i) = \sum_{j=0}^{n_i-1} \mathcal{C}_A(f_{ij}), \tag{42}$$

$$\mathcal{C}_e(v_i) = \sum_{j=0}^{n_i-1} \mathcal{C}_e(e_{ij}), \tag{43}$$

$$\mathcal{C}_n(v_i) = \sum_{j=0}^{n_i-1} \mathcal{C}_n(f_{ij}). \tag{44}$$

Next we have the two global constraints,

$$\mathcal{G}_A = A_l\left(A_{\text{tot}} - \sum_{i=0}^{N_v-1} A(v_i)\right)^2, \tag{45}$$

$$\mathcal{G}_V = V_l\left(V_{\text{tot}} - \sum_{i=0}^{N_v-1} V(v_i)\right)^2. \tag{46}$$

Both of these constraints serve to keep the total area and volume of the surface close to the fixed values A_{tot} and V_{tot}.

Another hidden constraint is that the total amount of each phase be fixed,

$$\frac{1}{A_{\text{tot}}} \sum_{i=0}^{N_v-1} \phi_i = P, \tag{47}$$

but this constraint is already imposed in the Monte-Carlo algorithm we use in the simulation. The total energy of the system is summarized as

$$\mathcal{H} = \mathcal{G}_A + \mathcal{G}_V + \sum_{i=0}^{N_v-1}\left[\frac{1}{2}\mathcal{H}_P(v_i) + \mathcal{H}_H(v_i) + \mathcal{H}_G(v_i)\right] + \sum_{i=0}^{N_v-1}[\mathcal{C}_A(v_i) + \mathcal{C}_e(v_i) + \mathcal{C}_n(v_i)]. \tag{48}$$

The factor of 1/2 is included in front of $\mathcal{H}_P$ to take into account that each piece of boundary is double counted.

F. Monte Carlo simulation

The Monte Carlo simulation works in two stages, one corresponding to phase exchanges and one corresponding to vertex movements [12].

Stage 1: For the phase exchanges we choose two vertices at random, v_i and v_j. If they have different phases ($\phi_i \neq \phi_j$) then we swap the two phases and calculate the change in energy using the discrete Hamiltonian defined above, ΔE. This procedure is then accepted with the probability $e^{-\Delta E/kT}$. If the move is rejected then the system is returned to the previous configuration. Since phases are only exchanged between vertices, the conservation of total phase is trivially imposed so long as the initial configuration has a specified phase fraction P.

Stage 2: Similarly, for the vertex movements we choose a random vertex v_i and a random unit direction in space $\vec{r}$. We then move the vertex a small distance (about 0.1% of the radius of the GUV) in that direction. All of the curvature and constraint fields are updated and the change in energy, ΔE, due to this perturbation is calculated. It is accepted with probability $e^{-\Delta E/kT}$. If it is rejected, then the vertex is moved back to its original position.

This procedure is iterated a large number of times (roughly $10\,000 \times N_v$ with phase exchanges and vertex movements performed in a 2:1 ratio) and annealed at a linear rate from high temperature until the system has achieved a minimal energy state to within thermal fluctuations. This minimal energy state defines the equilibrium morphology that we would expect to observe in experiments where GUVs have had adequate time to anneal.

IV. RESULTS AND DISCUSSION

A. Curvature and line tension can produce modulated phases

Implementing the discrete model outlined above yielded the appearance of modulated phases similar to those observed experimentally on GUVs in this four-component system. The simulation shows a strong periodic pattern arising from the competition between the line tension and curvature terms. Shown in Table I is the canonical parameter set that gives rise to a strong modulated phase pattern.

The parameters shown here were found by trial and error search of the parameter space. The bending moduli here are about one order of magnitude higher than the experimental values reported for some (different) lipid mixtures. The reported values put the typical bending moduli at values of

TABLE I. Canonical parameter set that is found to produce modulated phases.

Parameter	Value	Unit
γ	0.01	pN
κ_d	10×10^{-19}	J
κ_o	100×10^{-19}	J
$\bar{\kappa}_d$	-10×10^{-19}	J
$\bar{\kappa}_o$	-100×10^{-19}	J
R	25	μm
P	0.5	N/A

around $\kappa_d = 2 \times 10^{-19}$ J and $\kappa_o = 8 \times 10^{-19}$ J [14,15,18]. Notice that we have set $\kappa \approx -\bar{\kappa}$ for both the L_d and L_o phases in accordance with the observation that $\bar{\kappa}/\kappa \approx -0.9$ [26].

The line tension reported here is two orders of magnitude below typical experimentally reported values, $\gamma \approx 1.2$ pN [14,18]. Line tension values in our simulation of modulated phases should be smaller than those measured experimentally because the values of line tension reported in the literature correspond to large macroscopic domains (the shape and stability of macroscopic domains being the principle method of extracting this parameter).

We identify two reasons for this seeming discrepancy: First, line tension cannot be measured by any method yet reported in the regime of modulated phases. With near-certainty we can say that it must be much lower for such mixtures; second, given that we used only the bending energies as the interactions that oppose line tension, then if additional interactions are in play besides these bending energies, the line tension to produce modulated phase morphology would be larger. We are considering other potential long-range interactions (such as dipolar repulsion arising from the molecular structure of the lipids) to include in future simulations to test this hypothesis.

In order to ensure that the modulated phases are not an artifact in the simulation, we ran the simulation on much higher resolution lattices to see if the patterns persist. Figure 6 shows a side-by-side view of the patterns on a lattice containing 10 000 vertices and one containing 40 000 with the same parameter set. The poor scaling of the simulation with vertex number makes examination of much higher resolution problematic.

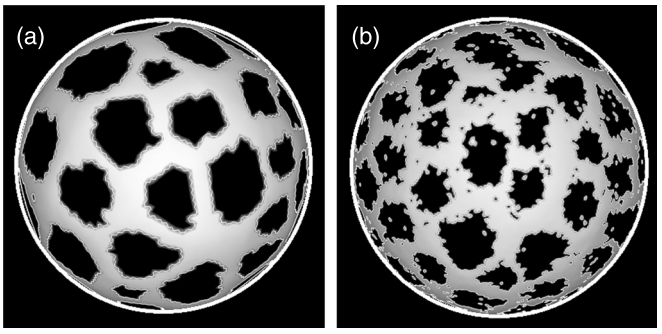

FIG. 6. Modulated phases can be simulated. Comparison of the pattern on a low resolution (10 000 vertex) lattice (a) to the pattern on a high resolution (40 000 vertex) lattice (b) shows that the patterning is not an artifact of the triangulation.

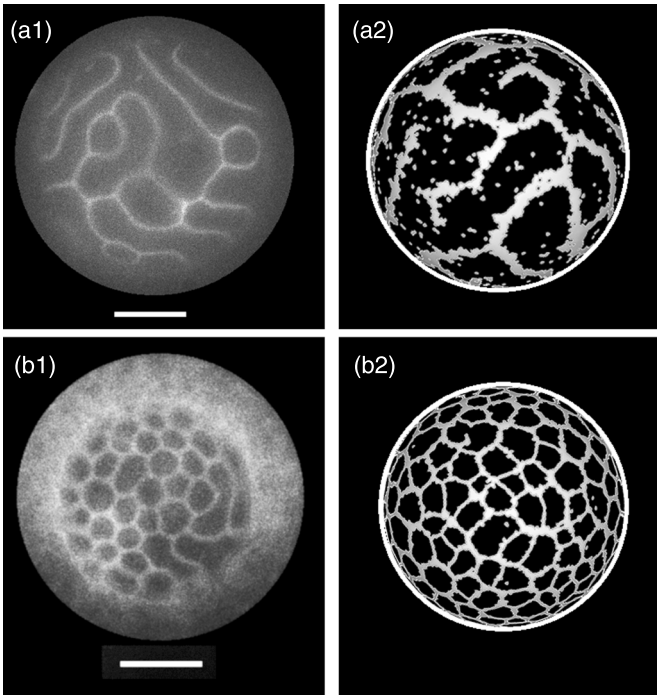

FIG. 7. Direct comparison of modulated phases observed experimentally on the surface of GUVs to patterns produced in simulation. (a) Simulation with $P = 0.75$ (a2) showing stripe-like patterns similar to those on an actual GUV (a1). (b) Simulation with $P = 0.75$ and $\kappa_o = -\bar{\kappa}_o = 300 \times 10^{-19}$J showing honeycomb patterns (b2). GUV in (a1) was taken from Fig. 1(c) for comparison with simulated GUV (a2). GUV composition (DSPC-DOPC-POPC-CHOL) in (b1) is 0.45/0.09/0.21/0.25. C12:0 DiI (0.02 mol%) was used in both (a1) and (b1). Scale bars 10 μm, temperature 23°C.

Figure 7 shows that with the same parameters as above, but with $P = 0.75$, simulated patterns very closely match experimental patterns observed on GUVs.

B. Modulated phases are thermodynamically stable

One important issue about modulated phases is whether or not the patterns are thermodynamically stable or instead are a kinetically trapped state. The minimal energy morphology of a phase-separated GUV in the absence of curvature is known to be a single round macroscopic domain [27], minimizing the perimeter-to-area ratio of the domain.

To determine the thermodynamic stability of the modulated phases we compared the energy of a single round domain morphology to that of a modulated phase morphology. We first artificially generated a GUV with a single round domain by turning off the shape exchange portion of our Monte Carlo simulation, and then we allowed the GUV to equilibrate. This gave a single round domain but did not contain the energetic contributions of the thermal fluctuations. To capture the thermal fluctuations we performed a second-stage equilibration where phase exchanges were turned off and the shape exchanges were allowed to equilibrate.

As Fig. 8 shows, the energy of the single round domain morphology exceeds that of the modulated phase morphology, indicating that the modulated phase morphology is more thermodynamically stable.

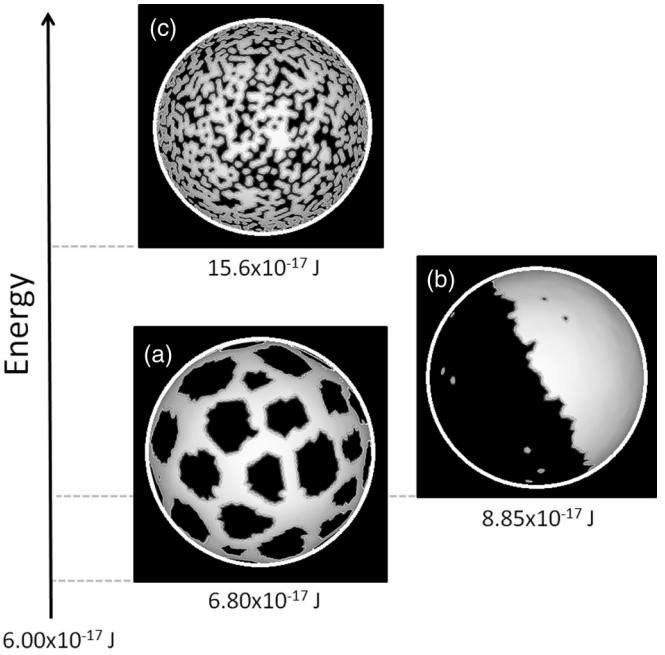

FIG. 8. With the parameters given in Table I, the modulated phase morphology (a) is the lowest energy state. The single round domain mophology (b) has higher energy, and the melted lattice (c) has the highest energy and most phase boundary.

All of the simulations shown here were started from a melted state (vertex phases randomly dispersed). A second test of the stability of the modulated phases was to start the system off in a single large domain state and then allow the system to relax to see if it still transitions to a modulated phase morphology. This process is shown in Fig. 9.

Starting from a macroscopically phase-separated GUV, a transition to modulated phases appears, again indicating that the modulated phases are thermodynamically more stable than the single round domain. Notice that the energy increases at the beginning of the simulation, seemingly in contradiction of the second law of thermodynamics. This is because we have plotted only the enthalpic part of the free energy, neglecting the increase in entropy as the domain begins to break apart.

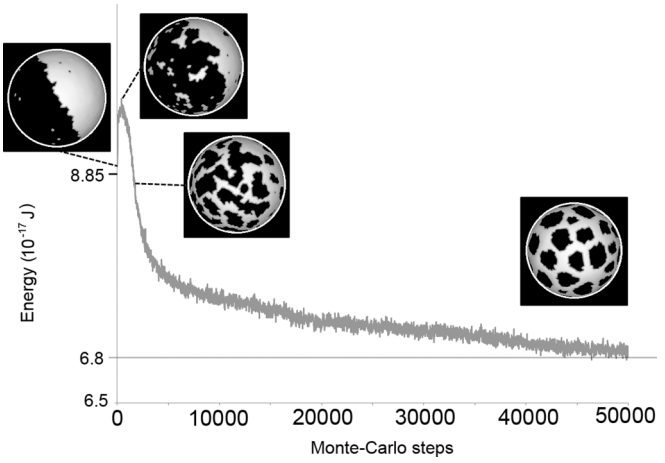

FIG. 9. Macroscopic domains transition to modulated phases. Energy as function of Monte-Carlo steps starting from a single macroscopic domain, which breaks up and eventually stabilizes to the modulated phase pattern. The simulation can take a long time to equilibrate as shown by the continually decreasing energy, but the pattern does not change appreciably in the tail end of the curve. The slight increase in energy at the beginning is probably compensated by the increase in entropy as the domain boundary begins to disintegrate.

C. The physical parameters of the phases and the GUV dictate the phase morphology

The simulation model shown here has seven tunable parameters, each affecting the energy landscape in some complex way. It is useful to do some exploration of how these parameters change the nature of the morphology. Moving along a tie line at a fixed value of ρ will only change the amount of each phase (P) on the surface without affecting any of the other parameters. This process is shown in Fig. 10 for three different values of P.

The line tension, γ, has a large effect on the phase morphology. The curvature and the line tension terms work in tandem to produce the modulated phases. If this balance is perturbed, the system abruptly transitions to a melted or macroscopically phase-separated morphology, Fig. 11.

At high line tension we noticed a large degree of kinetic trapping caused by the very large energy barrier to a single phase exchange. This caused nonequilibrium stabilization of multiple small domains. Kinetic trapping of domains by curvature is an experimentally observed phenomenon [28], but we are interested in studying equilibrium configurations.

The difference in bending rigidity between the L_o and L_d controls the width of the L_d lines and the size of the

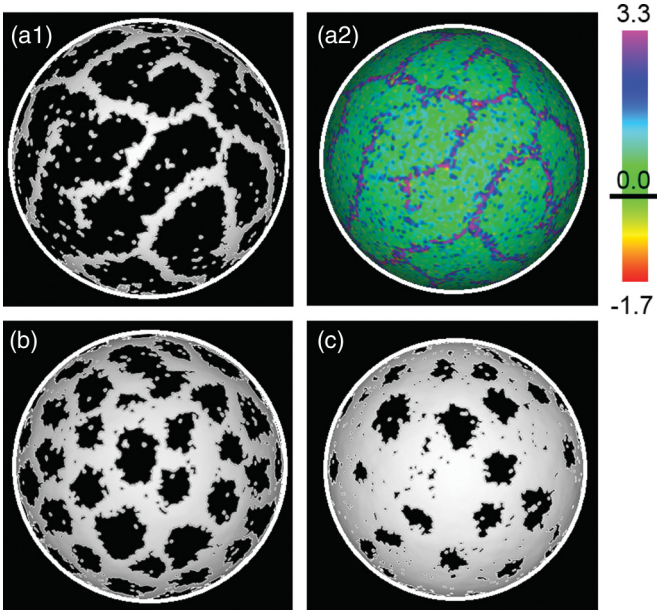

FIG. 10. (Color) Phase morphologies change as the phase fraction (P) is varied. (a1) $P = 0.75$; (a2) mean curvature map showing how the modulated phases and the geometry of the membrane couple. Curvature units in the color scale are μm^{-1}; (b) $P = 0.5$; (c) $P = 0.25$. The single pixel domains are not static structures but transiently flicker in and out of existence due to thermal fluctuations of the membrane shape in the L_o regions.

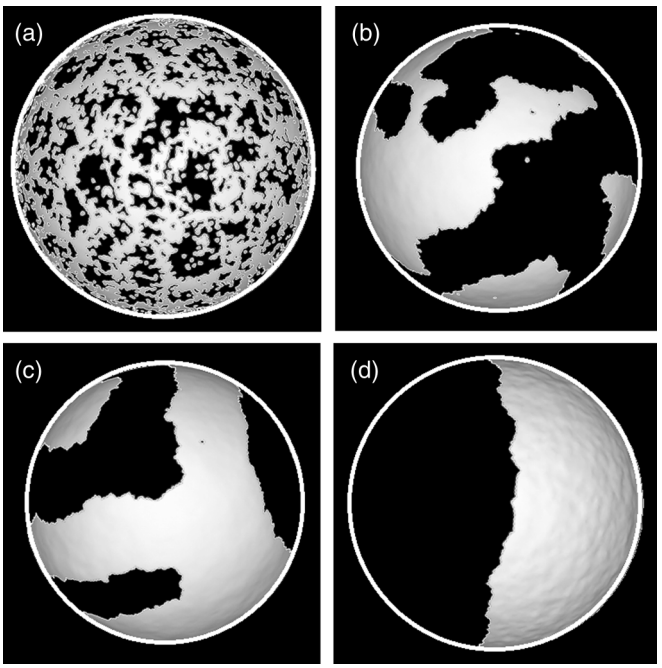

FIG. 11. Phase morphologies change as line tension is varied. (a) $\gamma = 0.005$ pN. (b) $\gamma = 0.02$ pN. (c) $\gamma = 0.03$ pN. (d) $\gamma = 1.5$ pN.

L_o domains. Figure 12 shows a series of increasing bending rigidity of the L_o phase while keeping moduli of the L_d phase fixed.

All of the simulations shown here are performed on $R =$ 25-μm GUVs. What affect, if any, does the size of the GUV have on the nature of the patterns? We find that scaling the radius of the GUV is energetically equivalent to scaling the line tension,

$$\mathcal{H}[R,\gamma] = \gamma L + \int_S \kappa(\phi)H^2 + \bar{\kappa}(\phi)GdA. \tag{49}$$

Scaling R by a factor a will scale all linear quantities by the same factor and all area quantities by a^2. Note that under this scaling the area fraction of each phase, P, is held fixed, so the actual area of each phase must change accordingly (by a factor of a^2).

$$\mathcal{H}[aR,\gamma] = \gamma(aL) + \int_S \kappa(\phi)(H/a)^2 + \bar{\kappa}(\phi)(G/a^2)(a^2dA), \tag{50}$$

$$= \gamma(aL) + \int_S \kappa(\phi)H^2 + \bar{\kappa}(\phi)GdA, \tag{51}$$

$$= \mathcal{H}[R,a\gamma]. \tag{52}$$

Thus, scaling the GUV size is equivalent to scaling the line tension, as in Fig. 11. See Supplemental Material for a detailed proof of these scaling relations [29].

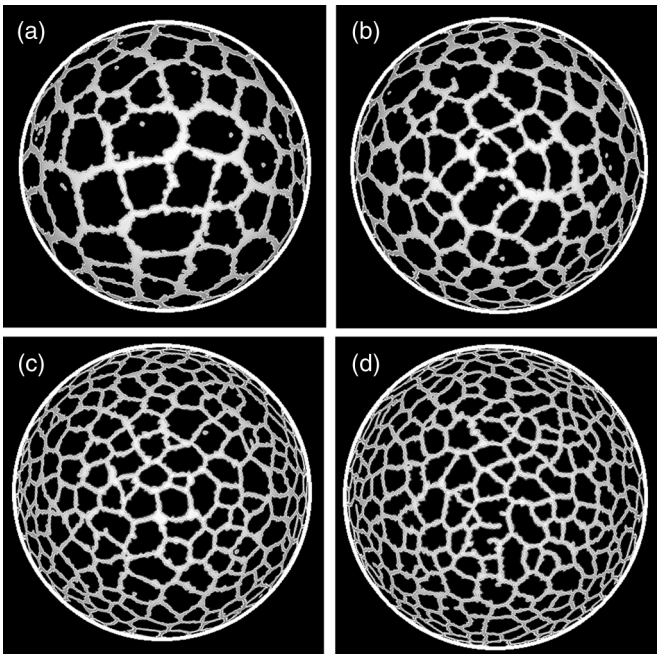

FIG. 12. Phase morphologies change as the bending moduli (κ_o and $\bar{\kappa}_o$) of the L_o phase are varied. (a) $\kappa_o = -\bar{\kappa}_o = 200 \times 10^{-19}$J. (b) $\kappa_o = -\bar{\kappa}_o = 300 \times 10^{-19}$J. (c) $\kappa_o = -\bar{\kappa}_o = 500 \times 10^{-19}$J. (d) $\kappa_o = -\bar{\kappa}_o = 1000 \times 10^{-19}$J.

V. CONCLUSION AND FUTURE DIRECTIONS

We have shown that the Helfrich model can explain the existence of modulated phase patterning: Patterns obtained through simulation closely match those experimentally observed on the surfaces of GUVs in the four-component system DSPC-DOPC-POPC-CHOL and represent thermodynamically stable configurations. The parameters of line tension and bending energies yield a range of different patterns (including striped, honeycomb, and macroscopic), depending on their relative and absolute values. This successful modeling provides a foundation for systematic study of the control of domain size in phase-separated biological membranes.

A. Future Studies

(1) Spherical topology can break the symmetry of the curvature fields. By performing simulations on flat planar lattices, we will examine if patterning persists.

(2) Accurate measurements of the various model parameters are central to relating our simulations to the experimental system. We plan to use the microscopy-based method used by Semrau *et al.* [14] to measure elastic parameters as a function of ρ in our four-component system. These experimentally determined parameters will enable us to test the validity and accuracy of the simulation in faithfully representing the energetics of phase separation in our four-component bilayer mixture.

(3) Membrane tension might have a strong influence on modulated phases. In all of the simulations shown here the global volume constraint, $\mathcal{G}_V$, is omitted to allow water to equilibrate across the membrane. Including a global volume constraint and setting the equilibrium volume, V_{tot}, lower or higher than that of a uniform sphere enables simulation of the changes in membrane tension caused by osmotic stress. We plan to compare such simulations with an experimental system where GUVs are subjected to a change in osmotic pressure across the membrane.

(4) Our model makes the strong prediction that the ratio of vesicle diameter to line tension is the key parameter,

along with bending energies, that control domain morphology. Studies are underway to verify the size and line tension scaling relation by correlating phase morphology with vesicle size, both experimentally and in simulations.

(5) The phase coexistence itself, as well as line tension and bending moduli, are sensitive to temperature. As a further study of modulated phase equilibrium, we will compare the temperature dependence found in the simulations with experimental observations of the temperature-controlled GUVs on the microscope stage.

ACKNOWLEDGMENTS

Support was from a research award from NSF MCB 0842839 (to G.W.F.). J.J.A. received support from NIH Training Grant No. 1-T32 GM 08267.

[1] J. Zhao, J. Wu, F. Heberle, T. Mills, P. Klawitter, G. Huang, G. Costanza, and G. Feigenson, Biochim. Biophys. Acta. **1768**, 2764 (2007).
[2] S. Veatch and S. Keller, Biochim. Biophys. Acta. **1746**, 172 (2005).
[3] F. Heberle, J. Wu, S. Goh, R. Petruzielo, and G. Feigenson, Biophys. J. **99**, 3309 (2010).
[4] F. A. Heberle, R. S. Petruzielo, J. Pan, P. Drazba, N. Kucerka, R. F. Standaert, G. W. Feigenson, and J. Katsaras, J. Am. Chem. Soc. (2013), doi: 10.1021/ja3113615.
[5] M. Swamy, L. Ciani, M. Ge, A. Smith, D. Holowka, B. Baird, and J. Freed, Biophys. J. **90**, 4452 (2006).
[6] P. Sengupta, D. Holowka, and B. Baird, Biophys. J. **92**, 3564 (2007).
[7] D. Lingwood and K. Simons, Science **327**, 46 (2010).
[8] T. Konyakhina, S. Goh, J. Amazon, F. Heberle, J. Wu, and G. Feigenson, Biophys. J. **101**, L08 (2011).
[9] P. Kingsley and G. Feigenson, Chem. Phys. Lipids **24**, 135 (1979).
[10] M. Seul and D. Andelman, Science **267**, 476 (1995).
[11] G. Arreaga, R. Capovilla, C. Chryssomalakos, and J. Guven, Phys. Rev. E **65**, 031801 (2002).
[12] J. Hu, T. Weikl, and R. Lipowsky, Soft Matter **7**, 6092 (2011).
[13] Y. Kaizuka and J. Groves, New J. Phys. **12**, 095001 (2010).
[14] S. Semrau, T. Idema, L. Holtzer, T. Schmidt, and C. Storm, Phys. Rev. Lett. **100**, 088101 (2008).
[15] D. Marsh, Chem. Phys. Lipids **144**, 146 (2006).
[16] Y. Yoon, J. Hale, P. Petrov, and P. Cicuta, J. Phys.: Condens. Matter **22**, 062101 (2010).
[17] J. Pecreaux, H. Dobereiner, J. Prost, J. Joanny, and P. Bassereau, Eur. Phys. J. E **13**, 277 (2004).
[18] T. Baumgart, S. Hess, and W. Webb, Nature (London) **425**, 821 (2003).
[19] J. Fan, M. Sammalkorpi, and M. Haataja, Phys. Rev. E **81**, 011908 (2010).
[20] A. Imperio and L. Reatto, J. Chem. Phys. **124**, 164712 (2006).
[21] A. Travesset, J. Chem. Phys. **125**, 084905 (2006).
[22] J. Liu, S. Qi, J. Groves, and A. Chakraborty, J. Phys. Chem. B **109**, 19960 (2005).
[23] S. Rozovsky, Y. Kaizuka, and J. Groves, J. Am. Chem. Soc. **127**, 36 (2005).
[24] F. Brown, Annu. Rev. Phys. Chem. **59**, 685 (2008).
[25] A. Hammond, F. Heberle, T. Baumgart, D. Holowka, B. Baird, and G. Feigenson, Proc. Natl. Acad. Sci. USA **102**, 6320 (2005).
[26] M. Hu, J. Briguglio, and M. Deserno, Biophys. J. **102**, 1403 (2012).
[27] S. A. Akimov, P. I. Kuzmin, J. Zimmerberg, and F. S. Cohen, Phys. Rev. E **75**, 011919 (2007).
[28] T. Ursell, W. Klug, and R. Phillips, Proc. Natl. Acad. Sci. USA **106**, 13301 (2009).
[29] See Supplemental Material at http://link.aps.org/supplemental/10.1103/PhysRevE.87.022708 for a detailed proof of these scaling relations.